Ocean Engineering 268 (2023) 113320

Contents lists available at ScienceDirect

Ocean Engineering

journal homepage: www.elsevier.com/locate/oceaneng

Validation of a CFD model for wave energy system dynamics in extreme waves

Eirini Katsidoniotaki [a,e,*], Zahra Shahroozi [a], Claes Eskilsson [b,c], Johannes Palm [d], Jens Engström [a], Malin Göteman [a,e]

[a] Department of Electrical Engineering, Uppsala University, Lägerhyddsvägen 1, SE-752 37 Uppsala, Sweden
[b] Renewable Energy Unit, RISE - Research Institutes of Sweden, Box 857, SE-501 15 Borås, Sweden
[c] Department of the Built Environment, Aalborg University, Thomas Manns Vej 23, DK-9220 Aalborg, Denmark
[d] Sigma Energy & Marine AB, Ekelundsgatan 1-3, SE-411 18 Gotenburg, Sweden
[e] Centre of Natural Hazards and Disaster Science (CNDS), Villavägen 16, SE-752 36 Uppsala, Sweden

ARTICLE INFO

Keywords:
Extreme waves
CFD
OpenFOAM
Validation model
Wave energy
Point-absorber

ABSTRACT

The design of wave energy converters should rely on numerical models that are able to estimate accurately the dynamics and loads in extreme wave conditions. A high-fidelity CFD model of a 1:30 scale point-absorber is developed and validated on experimental data. This work constitutes beyond the state-of-the-art validation study as the system is subjected to 50-year return period waves. Additionally, a new methodology that addresses the well-known challenge in CFD codes of mesh deformation is successfully applied and validated. The CFD model is evaluated in different conditions: wave-only, free decay, and wave–structure interaction. The results show that the extreme waves and the experimental setup of the wave energy converter are simulated within an accuracy of 2%. The developed high-fidelity model is able to capture the motion of the system and the force in the mooring line under extreme waves with satisfactory accuracy. The deviation between the numerical and corresponding experimental RAOs is lower than 7% for waves with smaller steepness. In higher waves, the deviation increases up to 10% due to the inevitable wave reflections and complex dynamics. The pitch motion presents a larger deviation, however, the pitch is of secondary importance for a point-absorber wave energy converter.

1. Introduction

Computational fluid dynamics (CFD) codes have been widely utilized for the modeling of wave energy converters (WECs) and become essential for the analysis beyond the limit of linear hydrodynamic validity. To date, the most widely used CFD-based approach is the incompressible two-phase Reynolds averaged Navier–Stokes simulations. The computational cost is higher compared to the low- and mid-fidelity numerical tools but the CFD models have the advantage of supporting non-linear waves, viscous effects, wave overtopping, large amplitude motions and thus they provide an accurate evaluation of the WEC's dynamics (Katsidoniatski et al., 2021). In addition, CFD codes have the potential to complement or replace the costly, time-consuming, and non-flexible experimental campaigns.

However, although the CFD modeling has been widely implemented for the analysis of vessels and offshore fixed structures, the implementation in WECs is not straightforward, i.e., there is still some uncertainty related to the setup of the numerical wave tank model. In fact, until the moment of writing this study, limited guidance is provided around the development of WECs. Therefore, it is highlighted the need for standardization in the numerical modeling practices for WEC applications (Ransley et al., 2020). Currently, the only official standard for the design-load analysis of WEC is given in IEC TS 62600-2. However, additional guidance can be obtained from standards related to the offshore wind and Oil & Gas industry. The research community has taken the initiative to release collaborative projects for model validation purposes and evaluation of the numerical tools. For instance, the Collaborative Computational Project in wave–structure Interaction (CCP-WSI) organizes workshops and blind-test campaigns with the purpose of bringing together numerical modelers with the goal of assessing current numerical methods and accelerating the development of numerical modeling standards (https://https://www.ccp-wsi.ac.uk/). Similar scope has the International Energy Agency Technology Collaboration Programme for

* Corresponding author at: Centre of Natural Hazards and Disaster Science (CNDS), Villavägen 16, SE-752 36 Uppsala, Sweden.
E-mail addresses: eirini.katsidoniotaki@angstrom.uu.se (E. Katsidoniotaki), zahra.shahroozi@angstrom.uu.se (Z. Shahroozi), claes.eskilsson@ri.se (C. Eskilsson), johannes.palm@sigma.se (J. Palm), jens.engstrom@angstrom.uu.se (J. Engström), malin.goteman@angstrom.uu.se (M. Göteman).

https://doi.org/10.1016/j.oceaneng.2022.113320
Received 12 February 2022; Received in revised form 14 November 2022; Accepted 27 November 2022
Available online 15 December 2022

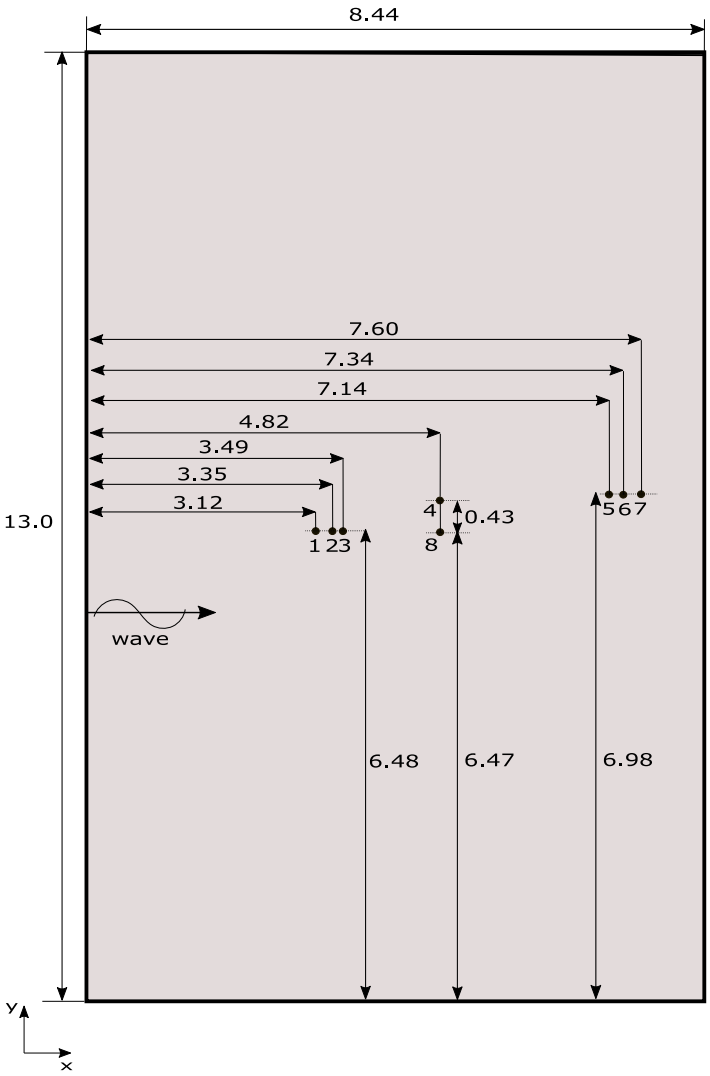

Fig. 1. Schematic view of the physical wave tank. All the dimensions are in meters. The enumerated points show the location of the wave gauges. The WEC is placed at point 8.

Ocean Energy Systems (OES) initiating the OES Wave Energy Converter Modeling Verification and Validation working group (https://www.ocean-energy-systems.org/). Also, experimental campaigns have been conducted under the framework of several academic projects. All the previous studies have concluded that the CFD results are shown to come in good agreement with the experimental tests.

A number of CFD validation studies against scaled experimental wave tank tests is found in the literature. Recent studies listed as follows; Kramer et al. (2021) provided a numerical model validation for heave decay tests of a sphere in the framework of the previously mentioned OES collaboration, participating in multiple research institutes and R&D companies. Mid- and high-fidelity numerical models were utilized by van Rij et al. (2021) to evaluate the responses of two taut-moored WEC-like buoys in focused waves. Windt et al. (2020b,c) presented an extensive validation study of a CFD-based numerical wave tank model for the 1:5 and 1:20 scale WaveStar point-absorber device, respectively. Ransley et al. (2019, 2020, 2021) presented the results of the CCP-WSI Blind Test Workshops in which the volunteers simulate a set of test cases based on bespoke physical tank tests without prior access to the measured data. Ransley et al. (2017) produced and validated the CFD model of a fixed and freely-pitching 1:10 scale model of the WaveStar. Palm et al. (2016) studied a coupled CFD-mooring analysis code for floating objects and validated the results against experimental tests. However, the CFD model validation on extreme wave conditions has not been widely considered.

According to IEC TS 62600-2, a wave energy converter should be designed considering the sea states along the 50-year environmental contour that provide the largest response. The cost of the wave energy is largely influenced by the extreme wave loads as mentioned by Neary et al. (2014) and Starling (2009), therefore, it is essential to examine the impacts from extreme events on the WECs. Recent studies have been focusing on the survivability of WECs in extreme waves conditions, utilizing CFD codes. Katsidoniotaki and Göteman (2022) simulated 100-year return period waves interacting with a WEC, using high-fidelity CFD model based on Reynolds-averaged Navier–Stokes (RANS) equations. They investigated the impact of alternating damping in the power-take-off system. Katsidoniotaki et al. (2021) investigated 50-year return period waves and their interaction with a point-absorber WEC. The authors utilized CFD simulations, based on RANS equations, to capture the highly non-linear effects; breaking waves and slamming loads. Ropero-Giralda et al. (2020) used Smoothed Particle Hydrodynamics (SPH) method to simulate a heaving point-absorber with a power-take-off system. They conducted a survivability study and examined the effects of highly energetic sea states. Coe et al. (2019) predicted extreme loading in a two-body WEC using a combination of mid and high-fidelity numerical modeling tools, while emphasizing in the need for increased experience especially in analyzing extreme conditions. van Rij et al. (2019) estimated the design loads for a WEC, considering the existing WEC design guidelines. Madhi

and Yeung (2018) studied practical solutions to increase the survivability of "The Berkeley Wedge" WEC utilizing the weakly compressible SPH method and model-scale experiments. The forces experienced in breaking-waves conditions were identified. Sjökvist et al. (2017) examined two different CFD models to validate a point-absorbing WEC in extreme wave. Chen et al. (2017) studied a point-absorber WEC in irregular and extreme waves utilizing a RANS-based CFD model. Hu et al. (2016) developed a methodology for extreme wave–structure simulation in OpenFOAM. These previous studies agree that high-fidelity models, like the one offered by CFD codes, are appropriate for capturing the hydrodynamic non-linearities and predicting accurately the extreme loading.

One of the most critical issues in WEC modeling using mesh-based CFD codes is the degradation of the computational mesh quality when the mesh is called to accommodate the large translational and rotational motion of the structure. Typically, the existing dynamic mesh motion methods can address this issue but limitations still persist. In particular, the morphing dynamic mesh method cannot handle responses that combine large translational and rotational motion, which is something expected to occur during extreme wave events. The overset dynamic mesh method can overcome this issue as shown by Katsidoniotaki and Göteman (2022), Windt et al. (2020a) and Chen et al. (2019). However, the overset method has some drawbacks related to the increased computational cost and the inferred complexity due to the interpolation process. Recently, Palm and Eskilsson (2021) introduced a modified morphing mesh method able to overcome the typical issue of the classic morphing mesh method for handling large motions. The method is less sensitive to the mesh design and able to accommodate large motions without affecting the overall mesh quality and adding extra computational cost.

This study aims to develop and validate the high-fidelity CFD model of a 1:30 scale point-absorber WEC based on the experimental wave tank campaign conducted in the Ocean and Coastal Engineering Laboratory, at Aalborg University, in Denmark. The WEC response and loads under 50-year return period extreme waves are estimated. The study follows the procedure of the experimental campaign. Initially, the extreme wave propagation is studied - without the presence of the WEC. Afterwards, decay tests are conducted and finally the wave–structure interaction is modeled. In this study, the innovative technique of the modified morphing mesh method (Palm and Eskilsson, 2021) that facilitates the CFD simulations of extreme wave–structure interaction is implemented and validated.

The remainder of the paper is organized as follows. Section 2 briefly describes the experimental setup, the WEC system and the examined waves. Section 3 outlines the test cases considered for the validation purposes. Section 4 provides the detailed description of CFD model, that is validated in this study. Section 5 presents, analyses and compares the numerical results with the experimental data, while the conclusions of this study are drawn in Section 6.

2. Experimental wave tank tests

A 1:30 scale wave tank experimental campaign, based on the full-scale Uppsala University WEC (Boström, 2011), is conducted in the Ocean and Coastal Engineering Laboratory at Aalborg University, in Denmark. The experimental setup and results have been presented previously by Z. Shahroozi (2021) and Shahroozi et al. (2022). Fig. 1 shows the schematic view of the wave basin, including all the relevant dimensions.

Fig. 2 shows the experimental setup which consists of a power take-off (PTO) system with linear friction damping and a cylindrical buoy with an ellipsoidal bottom. The PTO is made of a linear rod, a spring-compressed Teflon module that is rubbing against the linear rod for applying constant friction, and an upper end-stop. In this study, the PTO friction damping is 7.4 N and the PTO translator motion is restrained only by the upper end-stop and there is no lower end-stop in the system. The total upper-stroke length is defined as equal to 110 mm in order to capture the influence of full end-stop spring compression. The buoy and PTO properties are provided in Table 1 and Table 2, respectively. The mass, center of gravity (CoG), and moment of inertia are obtained from a computer-aided design (CAD) model, however, they have not been tested experimentally according to the procedure described by Hinrichsen (2014).

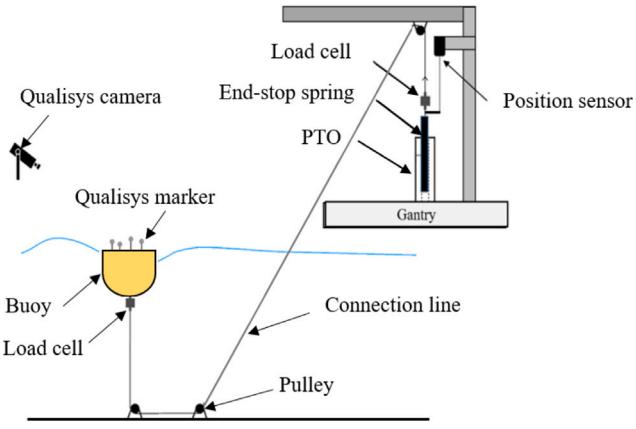

Fig. 2. Wave tank experiment sketch obtained by Shahroozi et al. (2022).

Table 1
Physical properties of the buoy.

Parameter	Unit	Value
Diameter	m	0.33
Height	m	0.38
Draft	m	0.23
Mass	kg	15.73 ± 0.001
Center of gravity	m	(0, 0, 0.1186)
Moment of inertia	kgm^2	(0.3537, 0.3537, 0.2918)

Table 2
Physical properties of the PTO.

Parameter	Unit	Value
Mass	kg	2.138 ± 0.001
Full upper-stroke length	m	0.110
End-stop spring coefficient	N/m	5900
End-stop spring uncompressed length	m	0.06
End-stop spring compressed length	m	0.028
Damping	N	7.4

The buoy position in six degrees of freedom is tracked by Qualisys with four cameras with a sampling rate of 300 Hz. The surface elevation is measured by eight wave gauges with a sampling frequency of 256 Hz: two in the vicinity of the buoy, three in the front, and three behind the buoy. The buoy is situated at 6.477 m and 6.540 m from the wave tank sidewalls and 4.819 m from the wavemaker. Two load cell devices are installed at the buoy and the PTO to measure the line force with a capacity of 2000 N. A wire draw line position sensor with a measurement range of up to 1000 ± 0.3 mm is used to measure the PTO translator position. The load cell and position sensor operate at 256 Hz sampling frequency. Photos from the experimental wave tank tests are shown in Fig. 3.

The experimental tests may include some uncertainty in the measurement of the PTO friction damping force and the mooring line force. More information can be found in Shahroozi et al. (2022).

(a) Empty wave tank test setup.

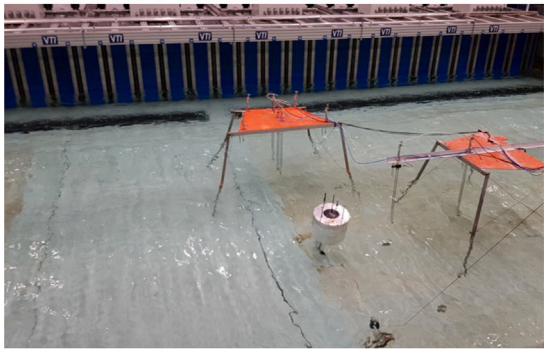

(b) Complete setup with buoy and wave gauges installed.

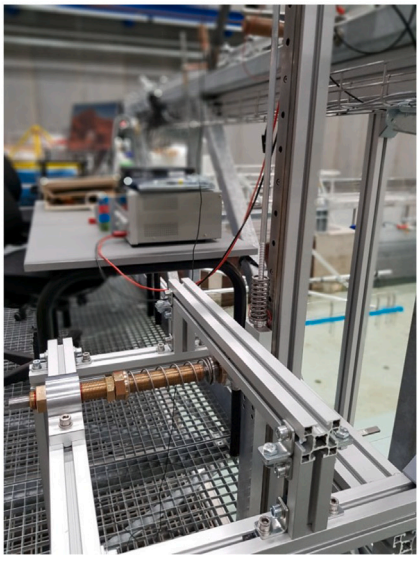

(c) PTO system.

Fig. 3. Experimental wave tank tests photos.

3. Test cases

3.1. Empty wave tank tests

Empty wave tank tests are performed to calibrate the waves and to determine their reproducibility given predetermined wave characteristics. The empty wave tank test includes eight wave gauges to measure the surface elevation without the presence of the WEC. The experimental basin is equipped with long-stroke segmented piston wave maker and active absorption.

The wave calibration is conducted for regular and focused waves, which are generated based on the sea state characteristics, i.e., JONSWAP wave spectrum, significant wave height, H_s, and peak wave period, T_p. The wave height and period of the regular waves are defined as $H = 1.9H_s$ and $T = T_p$, respectively. The value 1.9 comes from the assumption that during the extreme wave conditions, the wave height follows the Rayleigh distribution (Veritas, 2000; Yu et al., 2015). The focused waves are generated based on the Gaussian wave packet theory that considers the wave crest amplitude, A_n, the peak wave period, T_p, the standard deviation of the Gaussian amplitude spectrum, ϵ (Clauss and Bergmann, 1986), and the focal time, t_f, which is always 30 s. The wave characteristics of the examined sea states are summarized in Table 3. The wave steepness of the focused waves is denominated by kA_n and for regular waves by H/λ. The parameters k and λ refer to wavenumber and wavelength, respectively.

It is worth to highlight that the experimental records of the wave propagation may include uncertainty due to 20 ms lag in the Qualysis system. More information about the experimental wave generation can be found in Z. Shahroozi (2021) and Shahroozi et al. (2022).

3.2. Heave decay tests

The decay tests are essential for validating the convergence between the numerical and experimental setup of the model - without the influence of the incoming waves. Initially, only the buoy is included in the decay tests in order to examine whether its geometry is properly modeled. Afterward, the PTO is added in order to examine whether the numerical restraint matches the experimental PTO.

In the heave decay tests, the buoy is displaced from its equilibrium position and then released to oscillate freely. In the presence of PTO, the friction damping is set to the desired value of 7.4 N, and the buoy is pushed down to the water by pulling the PTO translator downward and then released. In the case of PTO absence, the buoy is simply pulled down to the water using the line rope and then released. There is not any particular setup for restraining the buoy from the other degrees of freedom, however, the buoy is pushed in the vertical direction with minimum movement in the other degrees of freedom.

3.3. Wave–structure interaction

The third stage of the experimental campaign studies the extreme waves interaction with the WEC system. At this point, some useful findings are summarized. First, it is not noticed compression of the upper end-stop spring during sea state 10. Conversely, a constant engagement of the end-stop spring is spotted for sea state 9 leading to non-linearities in the line force time series. The end-stop spring is significantly compressed during sea states 5a and 5b. Second, although both aforementioned focused waves are very high and steep, no wave breaking is observed during the wave tank experiment. Last, the mooring line force increases as the end-stop spring is compressed more frequently and with higher intensity. This behavior may be better comprehended through the PTO's equation of motion:

$$\mathrm{m_{PTO}}\ddot{\mathbf{z}} = \mathbf{F}_{\mathrm{line}} + \mathbf{F}_{\mathrm{end\text{-}stop}} + \mathbf{F}_{\mathrm{fPTO}} + \mathbf{F}_{\mathrm{fp}} + \mathrm{m_{PTO}}\mathbf{g} \quad (1)$$

where $\mathrm{m_{PTO}}$ is the PTO mass, including the mass of the load cell and other mechanical components connected to the PTO, $\ddot{\mathbf{z}}$ is the PTO acceleration, $\mathbf{F}_{\mathrm{line}}$ is the mooring line force, $\mathbf{F}_{\mathrm{end\text{-}stop}}$ is the force due to the compression of the end-stop spring, $\mathbf{F}_{\mathrm{fPTO}}$ is the friction PTO damping force, and $\mathbf{F}_{\mathrm{fp}}$ is the pulley friction force. All the bold characters refer to vector form.

Table 3
Parameters describing the examined waves.

Focused waves					
Sea state	A_n [m]	T_p [s]	H_s [m]	ϵ [1/m]	kA_n [–]
5a	0.17	1.64	0.18	0.72	0.296
5b	0.115	1.64	0.12	0.70	0.200
Regular waves					
Sea state	H [m]	T [s]	λ [m]	H/λ [–]	
9	0.22	1.52	3.20	0.068	
10	0.115	1.52	3.20	0.035	

4. Numerical wave tank

In this section, a high-fidelity numerical model is developed and implemented to study the extreme waves propagation and interaction with the WEC system. In this work, the open source CFD code OpenFOAM-v1906 is employed (ESI, 2019; Weller et al., 1998).

4.1. Numerical methods

The Reynolds Averaged Navier–Stokes (RANS) equations, describing the motion of an incompressible and isothermal Newtonian fluid, are expressed via the conservation of mass (Eq. (2)) and momentum (Eq. (3)):

$$\nabla \cdot \mathbf{V} = 0 \tag{2}$$

$$\frac{\partial(\rho \mathbf{V})}{\partial t} + \nabla \cdot (\rho \mathbf{V}\mathbf{V}) = -\nabla p + \nabla \cdot \mathbf{S} + \rho \mathbf{f}_b \tag{3}$$

where $\mathbf{V}$ denotes the three-dimensional velocity field, ρ is the density of the fluid, p is the pressure of the fluid, $\mathbf{S}$ is the viscous stress tensor and $\mathbf{f}_b$ includes the external forces.

The free water surface is captured using the volume of fluid method as described by Weller (2002). The phase fraction, α, is used to indicate the mixture between air ($\alpha = 0$) and water ($\alpha = 1$). The two-phase problem is treated as a single fluid and the local properties (density, ρ, and dynamic viscosity, μ) are then calculated from:

$$\rho = \alpha \rho_{water} + (1 - \alpha)\rho_{air} \tag{4}$$

$$\mu = \alpha \mu_{water} + (1 - \alpha)\mu_{air} \tag{5}$$

The conservation of the phase fraction is essential and an additional equation should be added to describe the motion of the phases:

$$\frac{\partial \alpha}{\partial t} + \nabla \cdot (\mathbf{V}\alpha) + \nabla \cdot (\mathbf{V}_c \alpha(1 - \alpha)) = 0 \tag{6}$$

where the last term is an artificial compression term and $\mathbf{V}_c = \min[c_\alpha |\mathbf{V}|, \max(|\mathbf{V}|)]$, where $c_\alpha = 1$. The multi-dimensional limiter for explicit solutions (MULES), as described by Rusche (2003), is implemented to ensure that $\alpha \in [0,1]$ and the interface compression scheme is used to maintain sharp interfaces during the CFD simulation.

The physical problem of wave–structure interaction leads to flow-induced boundary responses. Especially, the high and steep waves result in large WEC responses and the computational mesh has to accommodate these large deformations. OpenFOAM supports several types of dynamic mesh methods, which allow the computational mesh to change over the simulation time following the prescribed motion of the structure due to the interaction with the wave. More details about the dynamic mesh method utilized in this study are provided in Section 4.3.

In OpenFOAM, the *sixDoFRigidBodyMotion* library is used for solving the body's response in 6 degrees of freedom (DoF). In particular, the motion of the body is calculated via Newton's second law, considering the forces and moments due to the ocean wave's excitation and the additional external loads (i.e., PTO force). In the original mesh morphing method implemented in OpenFOAM, the deformation of the mesh is computed based on spherical interpolation (SLERP) in a deforming mesh region surrounding the moving wall boundary of the body.

The *interFoam* solver is used in the current study. In OpenFOAM-v1906, this solver can handle dynamic computational mesh and solve the three-dimensional RANS for incompressible phases using finite volume discretization and volume of fluid method. *interFoam* is a segregated solver and the PIMPLE algorithm is utilized for the pressure–velocity coupling.

4.1.1. Numerical restraint

In the *sixDoFRigidBodyMotion* library, the external forces acting on the body are modeled by means of a numerical restraint. In this study, the mooring line force is modeled based on the Eq. (1).

Fig. 2 shows the experimental setup that guides the mooring line from the buoy to the PTO and consists of three pulleys, i.e., one pulley is located at the gantry above the PTO, and two pulleys are submerged at the basin floor. The friction force from the pulleys is added to the mooring line force, as seen in Eq. (1). If the mooring line slides frictionless, the tension is constant along the line. In fact, there is friction due to spinning pulleys, and thus the tension varies along the mooring line and during the wave cycles. The measurements obtained from the experimental campaign show that the load cell located at the buoy and the load cell above the PTO show different values. When the translator is accelerated downwards, the buoy load cell measures greater force than the PTO load cell, whereas the opposite occurs when the translator is accelerated upwards,i.e., pulled by the buoy. The difference lies on the additional friction force due to the pulleys between the two load cells. Finally, this study considers the mooring line force measured by the buoy load cell because it is the force that determines the buoy's response in practice.

The magnitude of the friction force is different depending on the phase of wave cycle. The pulley friction is proportional to the normal force acting on the pulleys and that is proportional to the mooring line force. Considering a situation that the end-stop spring is not engaged, in the upward motion of the translator, the force due to its own weight and the PTO damping force act downwards (negative vertical direction). In the downward translator motion, the gravity force and the PTO damping force have opposite directions. In the former case the mooring line force appears to have greater value. Expressing the line force at the buoy load cell in terms of the line force at the load cell above the PTO, approximate values for the pulley friction force in Eq. (7) can be obtained,

$$F_{\text{fp}} \approx \mu \text{sign}(\dot{z}_{\text{PTO}}) \left(m_{\text{PTO}} g + F_{f\text{PTO}}\right) \left(c_1 \mu + \text{sign}(\dot{z}_{\text{PTO}}) c_2\right), \tag{7}$$

where μ is the friction coefficient of the pulleys and $\text{sign}(\dot{z}_{\text{PTO}}) = \pm 1$ depending on the upward or downward motion of the translator. The constants $c_1 \approx \sqrt{2} + \sqrt{3} + \sqrt{6} = 5.596$ and $c_2 \approx 1 + \sqrt{2} + \sqrt{3} = 4.146$ are geometrical constants that depend on the position and approximate line angles at the pulleys. Assuming a plausible friction coefficient of $\mu = 0.06$ based on Choi et al. (2017), values for the friction force are obtained as $F_{\text{fp}} \approx 7.06\ N$ when the translator is moving upwards, and $F_{\text{fp}} \approx -3.38\ N$ when the translator is moving downwards. The negative sign in the downwards motion indicates that the friction force always opposes the direction of motion. These values have been used as numerical input values for the pulley friction in the simulations, and shows good agreement with the experimental data. More information about pulley friction can be found in Z. Shahroozi (2021) and Shahroozi et al. (2022).

As a comparison, Z. Shahroozi (2021) analyzed the same experimental data and compared them to WEC-Sim results. In their work, the pulley friction was only included in the upward motion for the simulations, as they are more dominant in that direction of motion. Z. Shahroozi (2021) also measured the pulley friction experimentally in the upward motion, for the test case of sea state 10, and obtained a value of 7 N,

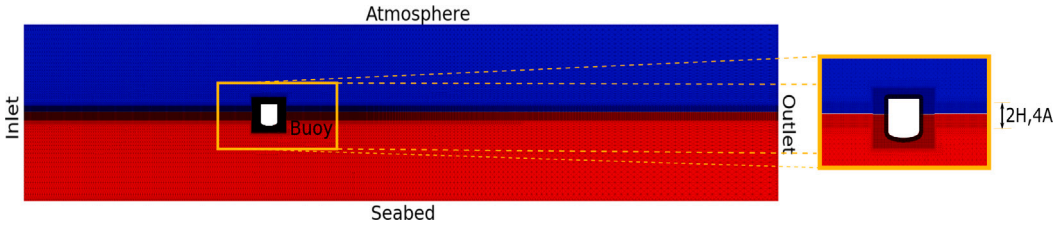

Fig. 4. Surface of the NWT in the xz plane, showing the computational mesh and the boundaries' labeling.

Table 4
OpenFOAM boundary conditions.

	Inlet/Outlet	Seabed	Atmosphere	Side walls	Buoy
alpha.water	waveAlpha/zeroGradient	zeroGradient	inletOutlet	zeroGradient	zeroGradient
pressure	fixedFluxPressure	fixedFluxPressure	totalPressure	fixedFluxPressure	fixedFluxPressure
velocity	waveVelocity	slip	pressureInletOutletVelocity	slip	movingWallVelocity
k	fixedValue/inletOutlet	kqRWallFunction	inletOutlet	zeroGradient	kqRWallFunction
ω	fixedValue/inletOutlet	omegaWallFunction	inletOutlet	zeroGradient	omegaWallFunction
nut	calculated	nutkWallFunction	calculated	calculated	nutkWallFunction
pointDisplacement	fixedValue	calculated	calculated	calculated	calculated

which is in agreement with the values obtained in this study. However, uncertainty may arise regarding the exact friction value during harsh sea states, i.e., sea states 5a, 5b and 9.

In the numerical restraint, the mooring line is considered massless with no resistance to the fluid. Additional inertia or friction forces that were present in the experimental tests are not captured in the numerical model.

4.2. Computational domain

The NWT is a rectangular box with dimensions 6 m × 14.82 m × 3 m (WxLxH). The width of the NWT is reduced and the distance between the buoy and the wave absorption boundary is extended compared to the experimental wave tank. The buoy is located at 4.82 m distance from the inlet boundary following the experimental settings.

The spatial discretization of the NWT follows the mesh convergence study presented in Katsidoniotaki and Göteman (2022) for the case of regular waves and Katsidoniotaki et al. (2021) for focused waves, securing discretization uncertainty below 3% and 1% respectively. Fig. 4 shows the structure of the computational mesh with the boundaries labeling. To capture the wave propagation without excessive damping, the region containing the free water surface is treated with higher resolution. As shown in Fig. 4, this region is extended to $2H$ and $4A$, where H is the regular wave height and A is the maximum crest amplitude of the focused wave. To reduce the computational cost, the cell-grading technique is applied. The cells are cubic (i.e., aspect ratio, AR = 1) up to 1.6 m downstream of the buoy position, but for the rest of the NWT's length the cells are stretched gradually until AR = 4. Along the NWT width, the cells are kept cubic up to $4R$ from the center of the buoy, where R is the radius of the buoy, but further this region the cells are stretched until AR = 3. Along the NWT height, the cells start to stretch above and below the higher-resolution interface region reaching AR = 2. The cubic area around the buoy with dimensions $4R{\times}4R{\times}3.6R$ consists of computational mesh that is additionally refined to capture the turbulence-related phenomena and the radiation–diffraction forces on the buoy.

In this study, the $k-\omega$ SST turbulence model is employed and wall functions are utilized to approximate the viscous effects in the boundary layer around the buoy, while the non-dimensional wall distance $y+ \in [30, 300]$. The boundaries' labeling is illustrated in Fig. 4, and the OpenFOAM specific boundary conditions are listed in Table 4. The adjustable time step follows the Courant–Friedrichs–Lewy (CLF) condition and maximum CLF number 0.50. The computational mesh size depends on the examined sea state and the number of cells ranges between 8.5 M and 14.3 M.

4.3. Modified morphing mesh method

The dynamic mesh motion of the floater was handled using the modified mesh morphing (MMM) approach suggested in Palm and Eskilsson (2021). For combinations of large surge and pitch motion, the original mesh morphing (MMO) algorithm presents limitations, which may result in bad results or crashed simulations, i.e.; see Palm and Eskilsson (2021) for a detailed discussion. The MMM method extends the functionality of the MMO by introducing a second cell motion deformation region corresponding to one or more of the translational degrees of freedom (DoF). The rotational DoFs are handled in the same way as in the original implementation. Two deformation regions are therefore introduced; an *inner region* that is defined by the inner (r_i) and outer (r_o) distance from the WEC's boundaries, and an *outer region* that allows the surge deformation of the entire inner bounding box. The surge (x) displacement is morphed from full surge amplitude at the interface to the inner region to no deformation and static mesh at a certain distance $|x| > x_o$ from the inner region. The remaining five degrees of freedom are handled inside the inner region as in the original method. By removing the surge motion from the inner deformation zone, a perfectly anti-symmetric cell deformation was achieved as a response to combined heave and pitch motion. This improved the stability of the numerical simulations leading to the successful simulation of the WEC's response under the focused wave groups.

To evaluate the MMM, the buoy's motion was compared against the equivalent results from the original method (MMO). The methods were evaluated for the test case of wave RW10. The normalized root-mean-square-error (NRMSE) is 2.96%, 2.27%, 4.0% for surge, heave and pitch motion, respectively. The pitch motion shows slightly higher deviation, but overall the errors are very small, thereby, the MMM is implemented for the rest of this study. The simulations were made with $[r_i, r_o, x_o]$ = [0.165 m, 1.0 m, 3.5 m] for FW5b and RW10, and [0.165 m, 1.0 m, 4.0 m] for FW5a and RW9.

4.4. Numerical wave generation and absorption

The IHFOAM toolbox is utilized for the wave generation and absorption, as described by Higuera et al. (2013). The static boundary method is applied for the wave generation at the inlet boundary of the NWT, while the active wave absorption allows the outlet boundary to cancel the incoming wave by applying an opposite uniform velocity profile.

For regular wave generation, the wave theory determines the wave velocity and surface elevation at the inlet boundary. For sea states 9 and 10, Stokes wave theory is implemented.

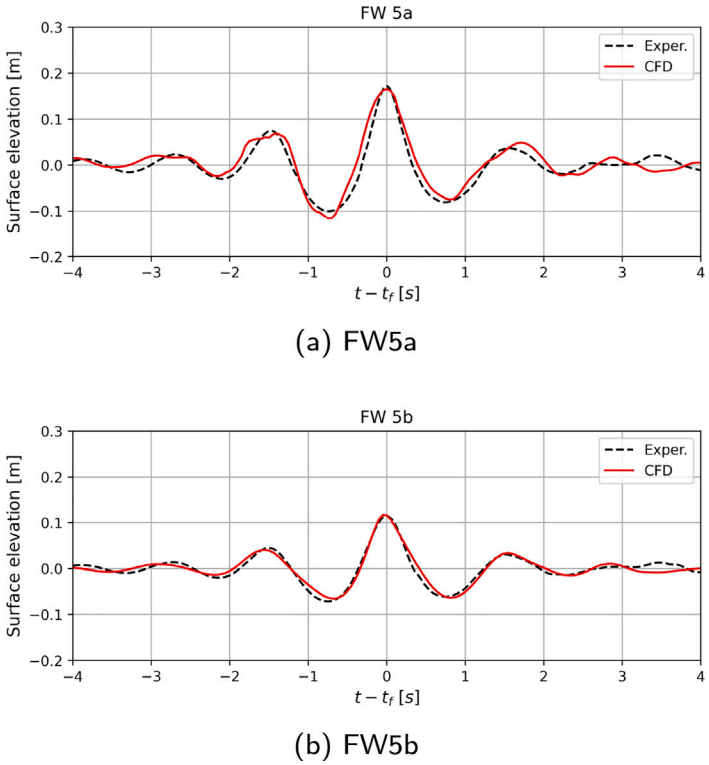

Fig. 5. Empty wave tank tests: Surface elevation at WG8 for the test cases of FW5a and FW5b.

The experimental focused wave generation follows the Gaussian wave packet theory (Clauss and Bergmann, 1986). A calibration procedure is followed to calibrate the numerical focused wave to match the experimental. The focused wave propagation is simulated in an empty NWT (i.e., the WEC is not included). Initially, the signal of the focused wave elevation recorded at the experimental WG2 is converted through Fast Fourier Transformation (FFT) into the sum of sinusoidal waves. The amplitude, frequency and phase of each wave component are defined and constitute the input for the numerical wave maker. After the first numerical wave modeling, FFT has performed again in the signal obtained from the numerical WG2. The sinusoids are now compared with the ones from the first FFT. The amplitudes are corrected by scaling with a factor which is the ratio of the amplitudes from the first and current FFT. The process is repeated until the experimental and numerical focused wave converges within an acceptable level.

5. Results and discussion

5.1. Empty wave tank tests

The wave generation in the NWT is compared and validated against the experimental wave tank (EWT) tests. The wave elevation is evaluated mainly at the WG8 (see Fig. 1), which is located at the position where the buoy will be placed later. To evaluate the temporal and spatial wave scatter, the wave gauges WG2, WG3, WG5 are additionally considered.

5.1.1. Focused waves

The numerical reproduction of steep focused waves is a very challenging task. In this study, the sea states 5a and 5b are represented as very high and steep focused waves, herein referred as FW5a and FW5b with their characteristics listed in Table 3. Specifically, the wave steepness (kA_n) is equal to 0.296 and 0.20 for FW5a and FW5b, respectively.

Fig. 5 shows the numerical solution for the numerical wave elevation compared to the experimental measurements at WG8. The results from the NWT and EWT modeling come in good agreement. The FW5b wave shows negligible variations, however, it is more difficult for the FW5a wave to be identically reproduced due to its higher steepness and the inevitable wave reflection effects in the experimental tests.

A set of assessment criteria is considered for better evaluation of critical wave characteristics; the maximum crest amplitude, the minimum preceding trough and the rising time are evaluated. Fig. 6 shows the values of the assessment criteria along with the estimated error, e, between the numerical and experimental values. The comparison confirm the good agreement between the experimental and numerical focused wave. The maximum crest amplitude is accurately captured ($e < 1\%$), while the preceding troughs present larger deviations, i.e., $e = 9.9\%$ and 2.86% for FW5a and FW5b, respectively. The main reason to suspect for this deviation lies on the seabed and outlet wall reflections. Particularly for the FW5a, the wave group consists of significant long-wave components that have already reflected back to WG8 by the point of the preceding trough.

5.1.2. Regular waves

The sea states 9 and 10 are represented as regular waves and their characteristics are listed in the Table 3. Herein, these waves are referred as RW9 and RW10, with wave steepness (H/λ) equal to 0.068 and 0.035, respectively. To evaluate the numerical wave reproduction, the phase-averaged surface elevation of ten consecutive wave periods, measured by the wave gauges WG2, WG3, WG8 (future buoy location), and WG5, is considered.

Spatial scatter of the free surface elevation commonly occurs due to wave dissipation and wave reflections from the tank side and end walls. In this study, the spatial scatter is evaluated by calculating the phase-averaged wave height at each wave gauge. The results are illustrated in Fig. 7. For better analysis, the wave at the WG3, WG8, and WG5 is compared with the WG2, with the latter being closer to the wavemaker. The normalized root mean square error (NRMSE) is used for the quantitative analysis, as defined in Eq. (8). Similar metric

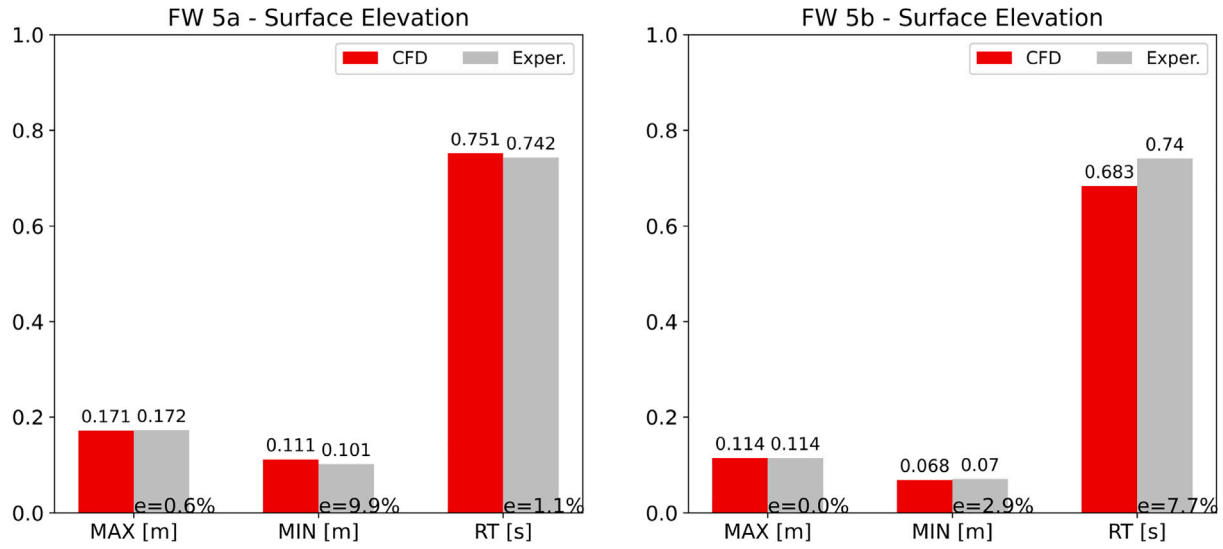

Fig. 6. Empty wave tank tests for FW5a and FW5b: The max crest (MAX), min preceding trough (MIN) and rising time (RT) for the surface elevation time series at WG8. The error, e, between the numerical and experimental values is shown.

Table 5
NRMSE of the phase-averaged wave height as measured from WG3, WG8, WG5 compared to WG2.

RW9	WG3	WG8	WG5
Experimental	0.033	0.097	0.048
CFD	0.007	0.055	0.083
RW10	WG3	WG8	WG5
Experimental	0.019	0.098	0.052
CFD	0.016	0.068	0.094

Table 6
NRMSE between the experimental and numerical phase-averaged wave height for empty wave tank tests.

Wave	WG2	WG3	WG8	WG5
RW9	0.022	0.037	0.018	0.040
RW10	0.023	0.034	0.008	0.036

Table 7
Comparison of natural period between experimental and CFD results.

Model	Exper. [s]	CFD [s]	Error [%]
Only Buoy	1.086	1.106	1.84
PTO included	1.067	1.055	1.12

is implemented for similar evaluation in Windt et al. (2020b).

$$NRMSE = \sqrt{\frac{\sum(\hat{y}-y)^2}{N}} \cdot \frac{1}{max(y)-min(y)} \tag{8}$$

where y is the wave height per wave cycle at WG2, $\hat{y}$ the wave height per wave cycle at WG3, WG8 or WG5, and N is the number of wave cycles. The results for the NRMSE are presented in Table 5. In the NWT, the effects of spatial scatter are less significant at the WG2-WG3 and WG2-WG8 proving stronger absorption capabilities. However, increased NRMSE is observed at WG2-WG5 due to numerical dissipation but this is not of particular interest as WG5 is located downstream the WG8. In the EWT, larger spatial scatter is observed and this might be due to the wave reflections from the end wall.

The temporal scatter of the free surface elevation is analyzed considering the standard deviation, σ, for ten consecutive wave periods, at each wave gauge. Fig. 7 shows also the σ, which is very small. The comparison between the EWT and NWT shows that the NWT exhibits less temporal scatter.

The free surface elevation is compared between the NWT and EWT. For a quantitative comparison, the NRMSE is calculated and the results are summarized in Table 6. In general, a good agreement is obtained, i.e., NRMSE $< 5\%$ for both RW9 and RW10. Especially at the WG8, where the buoy will be placed later, the NRMSE $< 2\%$. Higher NRMSE is noticed at WG5 because of the wave reflections and numerical dissipation.

5.2. Decay tests

Fig. 8 compares the numerical and experimental buoy motion during the heave decay tests and Table 7 compares the natural period of the system, with and without the PTO attachment. Table 8 provides the error in the upstroke/downstroke peaks of the oscillatory buoy motion.

5.2.1. Only buoy

As shown in Fig. 8(a), the simulated motion matches well with the experimental measurements. The error in natural period is $< 2\%$ (Table 7), and for the first three cycles, the error in peak values is $< 5\%$ (Table 8). However, the discrepancy is observed at the tail end of decay, showing a difference in the oscillation period and the value of the upstroke and downstroke peaks. The numerical error is accumulated during the simulation time resulting in larger deviation in the later wave cycles. In general, the heave motion from the experimental tests is slightly more damped than the CFD motion. A possible explanation can be attributed to the additional friction in the experiments.

5.2.2. PTO included

Fig. 15(a) shows that there is very good accuracy in terms of oscillation amplitude and the natural period of the system. The natural period comes approximately to 1% (Table 7) agreement between numerical and experimental tests. As summarized in Table 8, the error in the upstroke peaks is $\lesssim 1\%$. A significant deviation is recorded in the downstroke value of the second cycle. The numerical time series gives a deeper plunge in the second cycle due to friction effects, which might not have been all considered in the CFD simulations.

5.3. Wave–structure interaction

This section presents compares and discusses the results from the wave–structure interaction in the EWT and NWT tests.

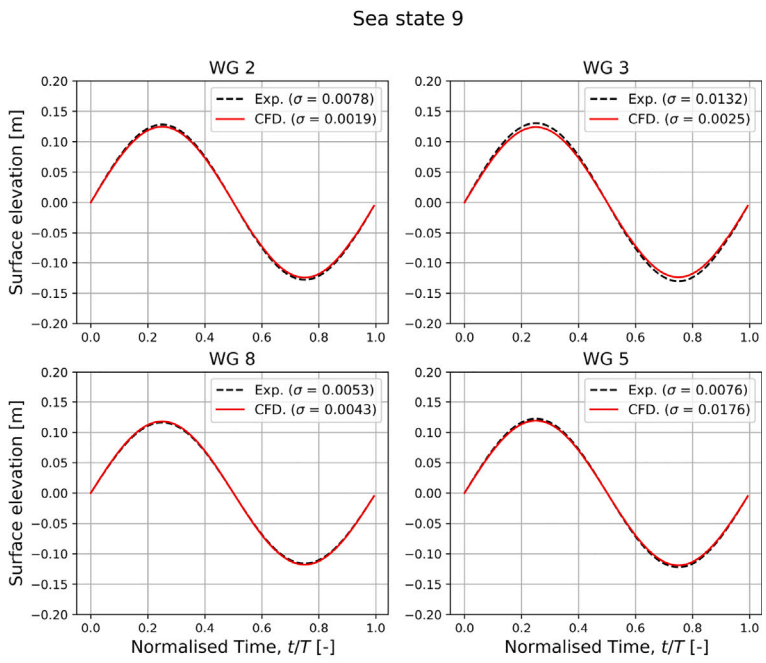

(a) Sea state 9

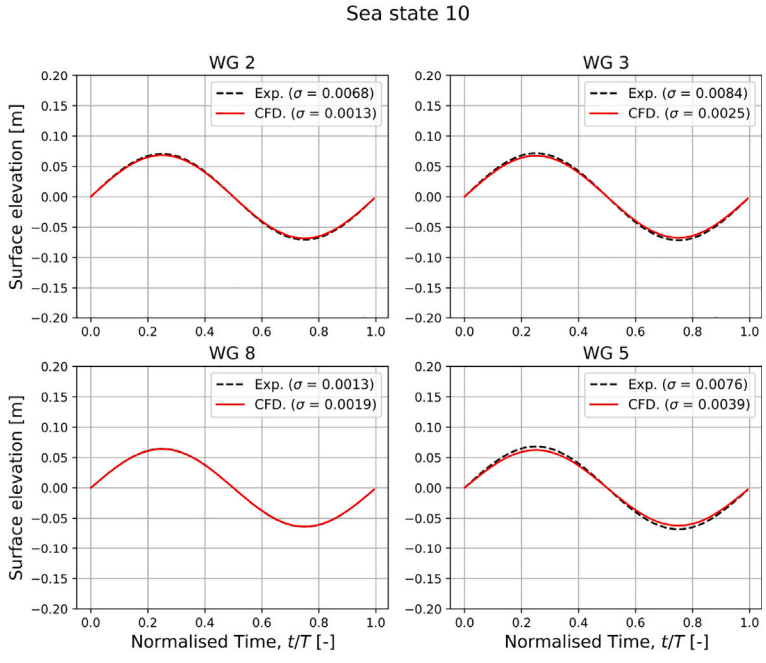

(b) Sea state 10

Fig. 7. Phase-averaged free-surface elevation for sea states 9 and 10 at WG2, WG3, WG5 and WG8.

5.3.1. Focused waves

Figs. 9 and 10 present a qualitative comparison of the numerical and experimental response for the WEC subjected to the focused waves FW5a and FW5b, respectively. Fig. 11 shows the WEC prior, during and after the wave FW5b focal time, t_f. From a visual inspection of Fig. 9(a) and Fig. 10(a), the numerical and experimental heave and surge response agree until the maximum peak, afterward, they present large deviation. However, the numerical modeling of the wave FW5b presents better convergence than wave FW5a. In general, wave steepness is a critical factor in accurate wave reproduction, i.e.; the wave FW5a is higher, steeper, and involves stronger nonlinear effects, therefore, it is more difficult to be modeled. Further explanation of the divergence between the numerical and experimental solution can be attributed to the wave reflections in the experimental tests which were provoked due to the small dimensions of the wave tank facility given the extreme nature of the examined waves. Another reason accounts for the drift forces which play a significant role in the surge motion; after the main wave-crest has passed, the presence of the higher order nonlinearities in drift force constitutes a numerical challenge which may explain the spread in the surge motion. However, as mentioned

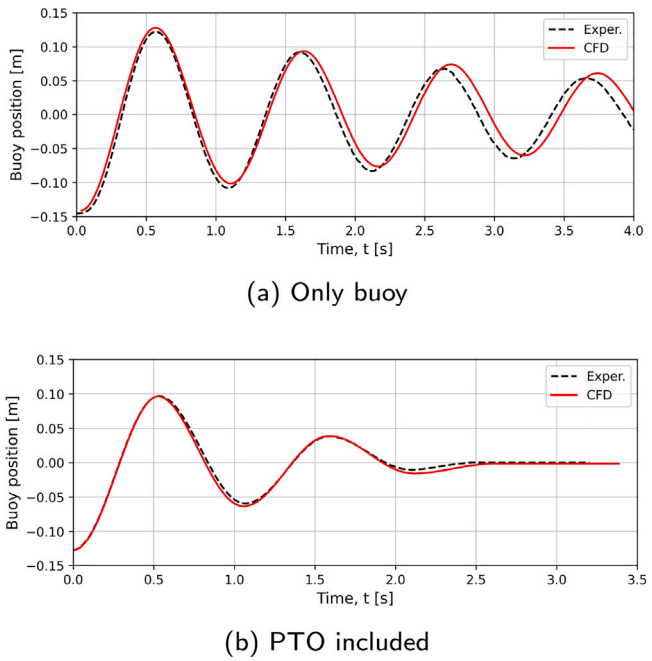

Fig. 8. Time series of the decay tests comparing numerical and experimental results for the heave buoy motion.

Table 8
Error [%] between the experimental and numerical values of the upstroke/downstroke peaks for each cycle.

Cycle	$Error_{upstroke}[\%]$	$Error_{downstroke}[\%]$
Only buoy		
1st	1.81	2.74
2nd	2.09	3.71
3rd	3.78	0.87
PTO included		
1st	0.39	6.71
2nd	1.07	49.23

in Windt et al. (2020d), the focused wave experiments are typically performed to calculate extreme loads which occur at the peak amplitude of the input wave, therefore, a deteriorating simulation accuracy after the peak event is less important than ensuring high accuracy leading up and during the peak. Larger deviations are noticed in the pitch motion, which is susceptible to the buoy characteristics, e.g.; center of gravity, center of rotation, moment of inertia. As previously mentioned, these values have been estimated based on the CAD model, and no validation procedure was conducted during the experimental campaign. Therefore, their accurate definition is prone to experimental uncertainty and any deviation from the real values can cause the observed deviation between the numerical and experimental pitch motion.

In terms of mooring force, Fig. 9(b) shows that the prediction come in better agreement, with the main and subsequent peaks being well-captured. Also from Fig. 10(b) it can be seen that the numerical mooring force is successfully captured, predicting accurately the main peak. The presence of the peaks is due to the compression of the upper end-stop spring in the PTO, adding extra force to the mooring line. However, the experimental signal shows second-order effects and oscillations which are not captured by the numerical restraint. The main reason is that the restraint is rather simplified.

For the quantitative comparison between the experimental and numerical results, three assessment criteria are evaluated; the maximum value, the minimum preceding trough and the rising time. The pitch motion is not included in this comparison, as uncertainty has been noticed regarding its proper simulation. Their comparison is illustrated in Fig. 12, proving that for the test case of FW5b, the motion of the WEC is predicted with e $\leqslant$ 12%. For the case of FW5a, the surge motion presents higher deviation, while the heave motion is captured relatively well. This larger error is likely because FW5a is steeper than FW5b, therefore, nonlinear wave dynamics play a greater role in the steeper waves. Moreover, looking back at Section 5.1, the simulated waves do not perfectly model the target experimental wave, especially for FW5a, and it likely leads to this divergence.

In Fig. 13, the heave-RAO, surge-RAO, and the maximum mooring force are compared. The RAO stands for the response amplitude operator and it is an engineering statistic that is used to determine the likely behavior of the WEC under the operation at sea states. In our study, the RAO is defined as the ratio of the WEC's maximum motion or load to the wave amplitude causing that response, i.e.; maximum crest amplitude. For FW5b the RAOs present a small error (e $\leqslant$ 3.0%), while for FW5a the error in RAOs increases up to 10.7%. In terms of the maximum force in the mooring line, it is predicted with e $\leqslant$ 7.0%. The reason of the good prediction relies on the fact that the peaks in the mooring force are mainly driven by the crests of the heave buoy motion. For the steep wave FW5a, the relatively small error in the maximum heave amplitude (e = 4.4%) explains the ability of the numerical model to provide the maximum force with 7.0% error. At this point, an additional statement drawn is that the milder sea state expressed as FW5b gives a larger heave-RAO maintaining the load in the mooring at lower level.

5.3.2. Regular waves

A qualitative comparison of the numerical and experimental WEC response and mooring force is presented. Figs. 14 and 15 refer to RW9 and RW10 waves, respectively. Before starting the analysis, it is useful for the reader to remember that the wave RW9 is higher and almost two times steeper than the wave RW10. Fig. 16 illustrates the buoy motion, subjected to RW9 wave during a wave cycle.

Table 9 presents the quantitative comparison of the numerical and experimental results using the NRMSE metric. Good quantitative agreement is found (NRMSE < 8%) in the free surface elevation measured at WG2, WG3 and WG4. Particularly at WG4, which is located in the same distance from the wave-maker as the WEC, the numerical wave is underestimated just by 5%. However, the deviation in the numerical and experimental waves is larger compared to the previous case of empty wave tank tests. The reason is that the interaction between the radiated and diffracted waves is now enhanced due to the presence of WEC. Therefore, the deviation in the WEC response is a rational consequence. In fact, the peaks in the heave motion come in good agreement with the experimental peaks, however, the numerical troughs are underestimated. The studied waves are in the region of intermediate water depth, i.e.; the seabed strongly affects the shape of the wave troughs due to friction effects. Steeper waves are significantly more susceptible to seabed friction effects. Overall, the NRMSE is 14% for heave motion in the RW9 wave. In the surge motion, an offset between the numerical and experimental time series is observed and the NRMSE is equal to 11%. The phase for both the heave and surge motion sequence is captured well. On the other side, the numerical model does not succeed in pitch motion. Higher errors in pitch motion have been mentioned in several similar applications (Ransley et al., 2021; Windt et al., 2020d; Domínguez et al., 2019).

In the mooring force records, it is observed that the PTO upper end-stop spring is compressed at every wave cycle and that explains the presence of peak forces. Although the numerical model overpredicts the peak forces with the NRMSE being equal to 20%, the time sequence phase is well-captured. The overestimation can partially lie on the larger offset in the surge motion (Fig. 14(a)-surge motion). Another possible reason can be attributed to the fact that the numerical model is not able to accurately account for the exact experimental setup. For instance, the mooring line is not fully stretched at some time intervals

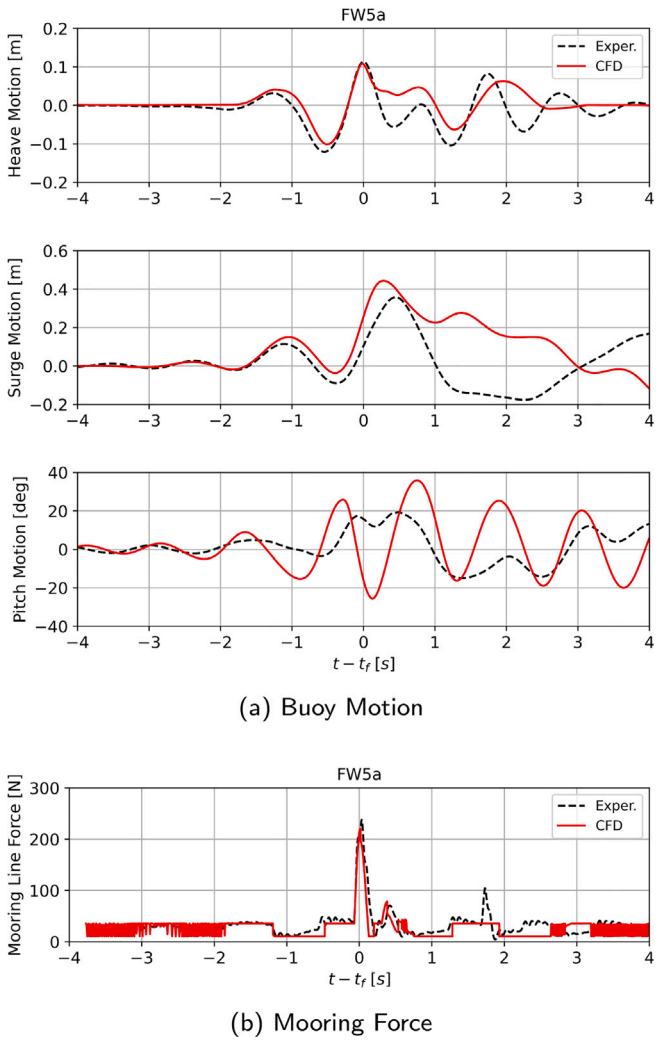

Fig. 9. Motion and force time series for WEC exposed to FW5a.

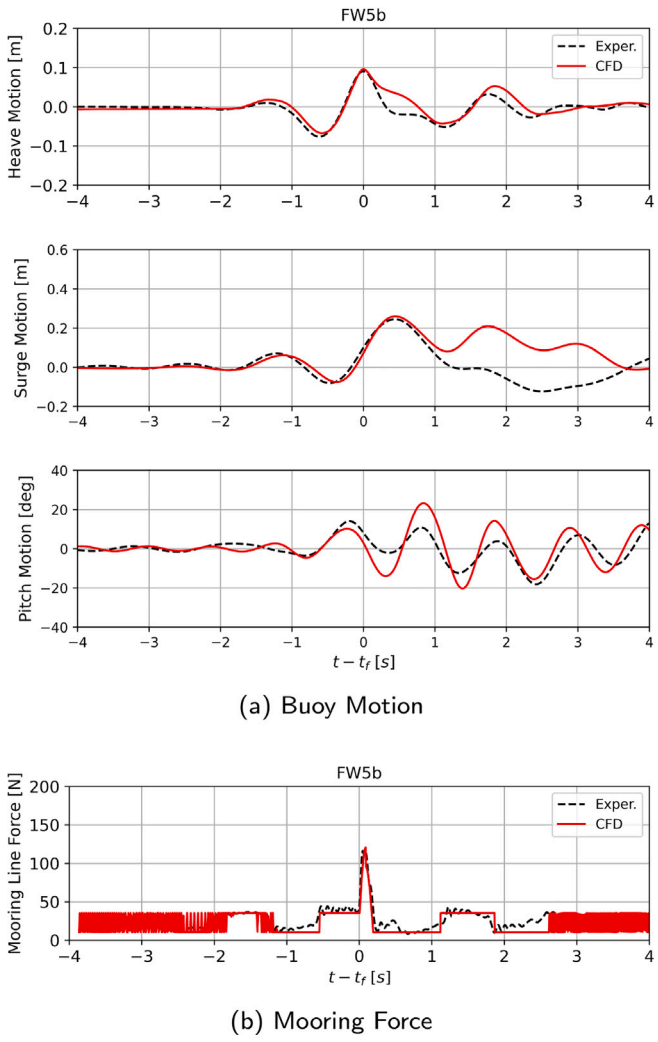

Fig. 10. Motion and force time series for WEC exposed to FW5b.

during the experimental tests, and this results in a decrease in the expected buoy motion.

The test case of RW10 gives better agreement in the comparison with the NRMSE being 5% and 10% for the heave and surge motion, respectively. The pitch motion is not successfully predicted neither for the RW10. From the mooring line trace, it is obvious that when the WEC is exposed to RW10 the upper end-stop spring is never compressed. The maximum force is accurately captured (NRMSE $< 5\%$).

Fig. 17 compares the heave-RAO, surge-RAO, and maximum mooring force. The results show that the numerical and experimental RAOs deviate less than 7%. In addition, the maximum mooring force is accurately predicted (e $\leqslant$ 5%). The Fig. 17 reveals that the WEC under the RW10 wave, which represents a milder sea state, performs better, i.e., the heave-RAO is higher while the mooring line experiences smaller loading.

5.4. Center of gravity sensitivity study

In experimental campaigns, there is always uncertainty about the exact value of several quantities. The uncertainty about the exact position of the buoy's center of gravity (CoG) is considered a possible reason for the deviation between the experimental and numerical pitch motion. The results have been presented in this study consider the CoG located at [0, 0, 118.6] mm. In this section, a sensitivity study is conducted considering that the CoG is displaced above and below its initial position by 5%, 10%, and 20%, i.e.; in total six cases are examined. In the present sensitivity study, the WEC is subjected to wave RW10.

Table 9
NRMSE between numerical and experimental data for sea states 9 and 10.

	RW9	RW10
Free surface elevation		
WG2	0.08	0.07
WG3	0.05	0.05
WG4	0.05	0.04
WG5	0.14	0.15
Buoy Response		
Heave	0.14	0.05
Surge	0.11	0.10
Force		
Mooring force	0.20	0.04

Fig. 18 shows the NRMSE between the originally defined CoG and each of the six examined cases expressing the error in heave, surge, and pitch motion of the WEC. The heave motion is the less affected motion in the change of CoG, while the surge and especially the pitch motion are significantly more affected. In particular, the surge motion can deviate up to 12.5%, while the pitch motion up to approximately 20%. From this sensitivity study, it is concluded that the surge and pitch

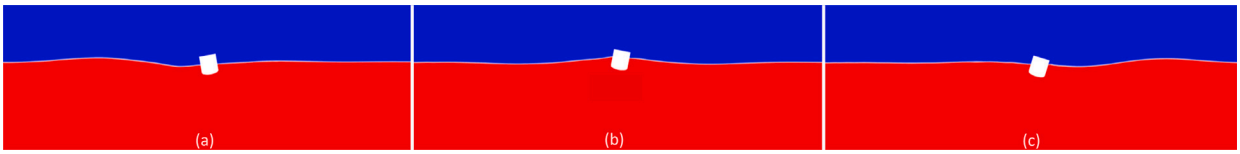

Fig. 11. WEC's response at (a) 1 s prior t_f, (b) t_f, (c) 1 s after t_f, when subjected to focused wave FW5b.

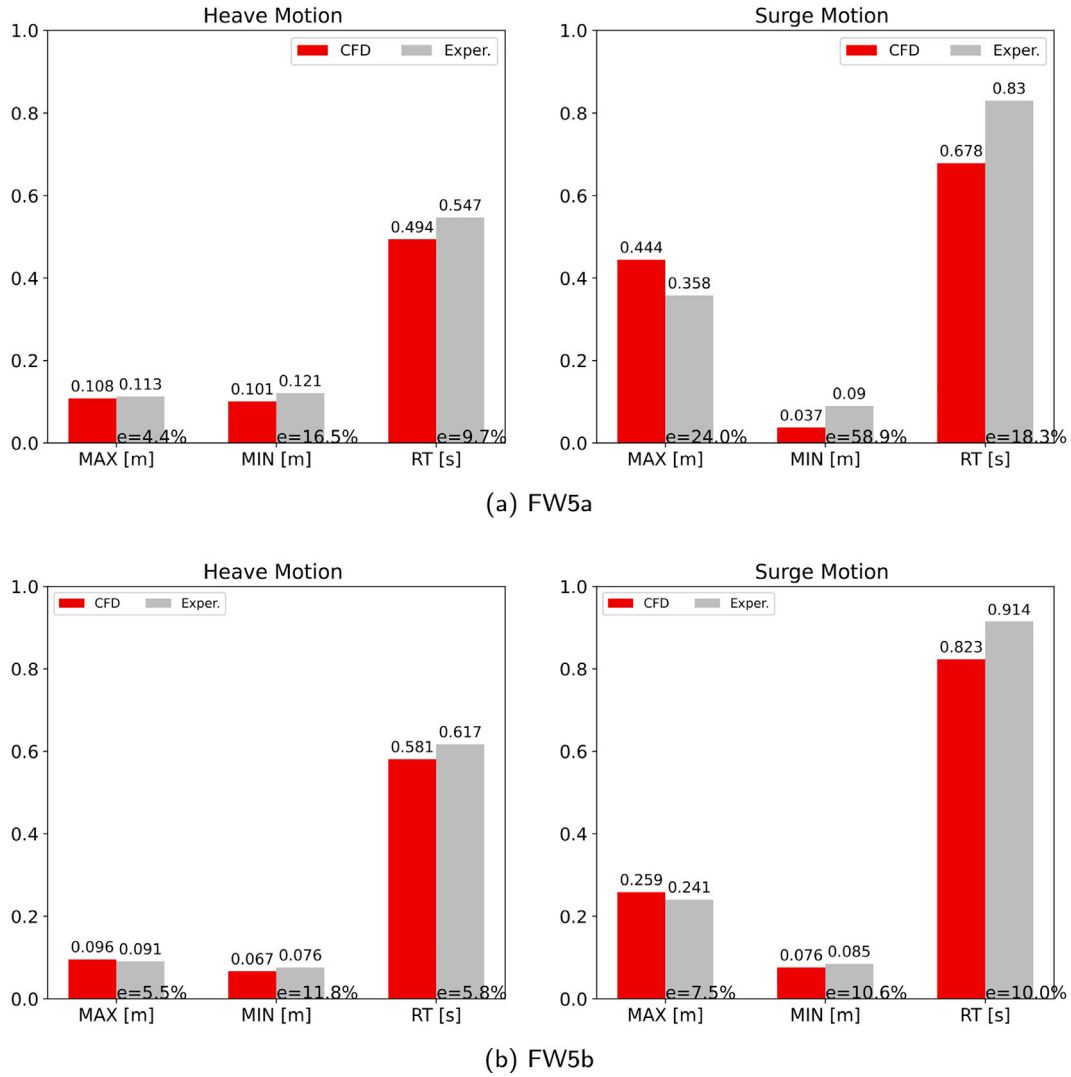

Fig. 12. Illustration of the max value (MAX), min preceding value (MIN) and rising time (RT) for the heave, surge subjected to wave (a) FW5a, (b) FW5b. The CFD and experimental results are compared.

motion can significantly differ with the change in the CoG, especially when it is displaced higher than the initial assumption.

6. Conclusions

This is a validation study of the numerical model developed for a 1:30 scale WEC operating in extreme waves. The model is validated on data from the experimental campaign conducted at Aalborg University, in Denmark. The examined WEC is a point-absorber subjected to 50-year return period waves which are modeled as regular and focused wave episodes.

A high-fidelity CFD model is developed to simulate the extreme wave–structure interaction and estimate the WEC motion in heave - surge - pitch and the mooring line force. The well-known issue of degradation in the computational mesh quality is expected to occur due to the large-amplitude response of the WEC in extreme waves. To combat this issue, the current study successfully implements and validates the morphing mesh method which is a novel version of the standard morphing mesh method in OpenFOAM.

Based on the results, it is concluded that the numerical model captures the WEC dynamics and forces with satisfactory accuracy. While the exact knowledge of the experimental facility is difficult to be determined, many assumptions were considered in the framework of the present study which may affect the results. Despite the wave reflections observed in the experimental data, the numerical wave elevation is reproduced with good agreement to the experiments (< 2% error), even for the cases of very steep waves. Additionally, the CFD model successfully reproduces the heave, surge motion and the mooring line force. Deviation lower than 7% is observed between the numerical and experimental RAOs for the WEC subjected in smaller

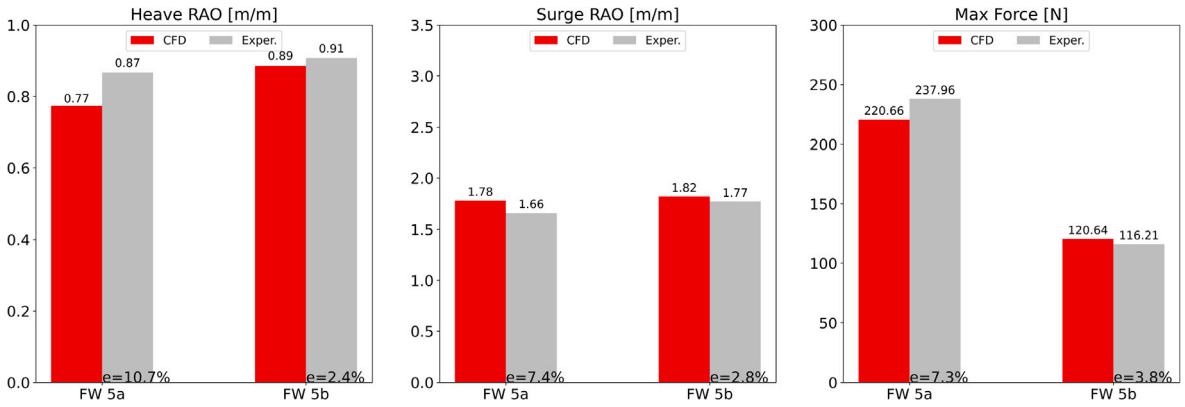

Fig. 13. Focused waves 5a and 5b: The heave, surge RAOs and the max. mooring force, for the numerical simulations and experimental results.

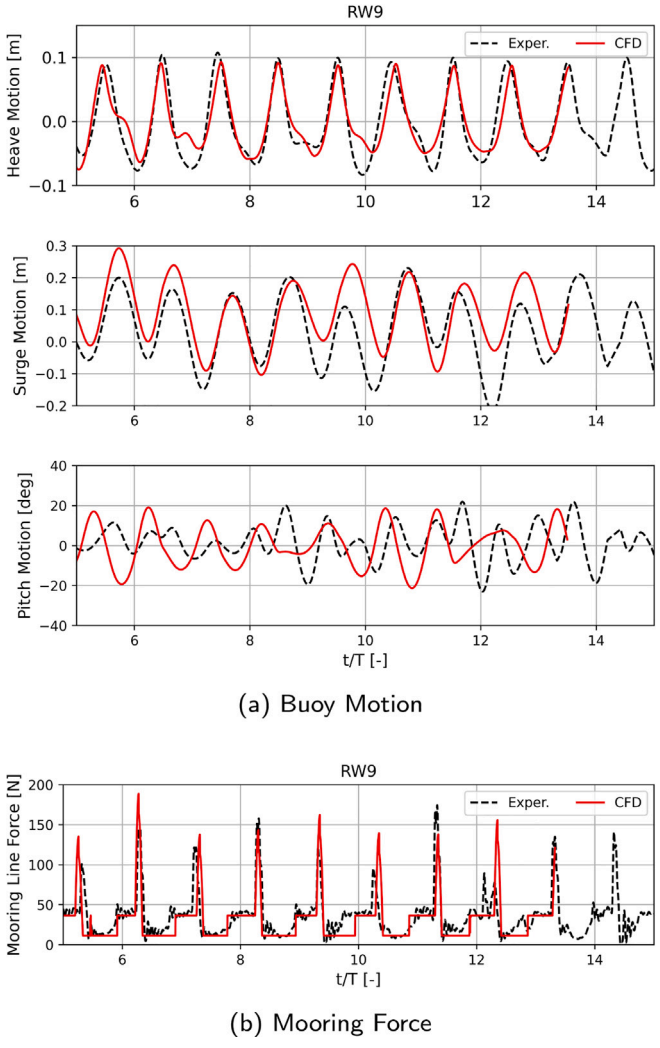

Fig. 14. Motion and force time series for WEC exposed to RW9.

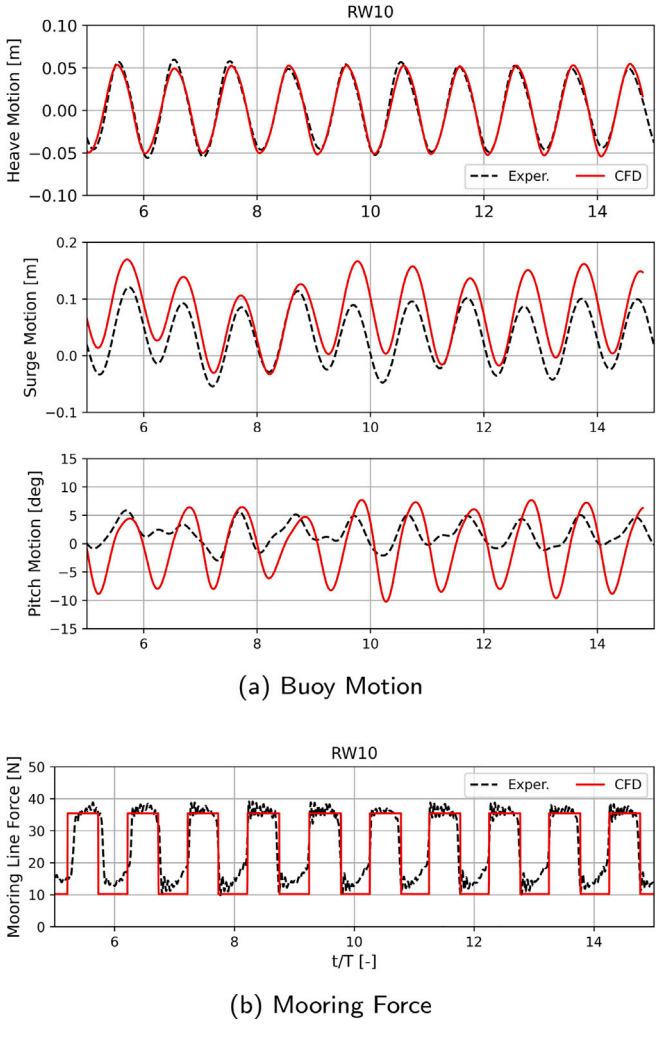

Fig. 15. Motion and force time series for WEC exposed to RW10.

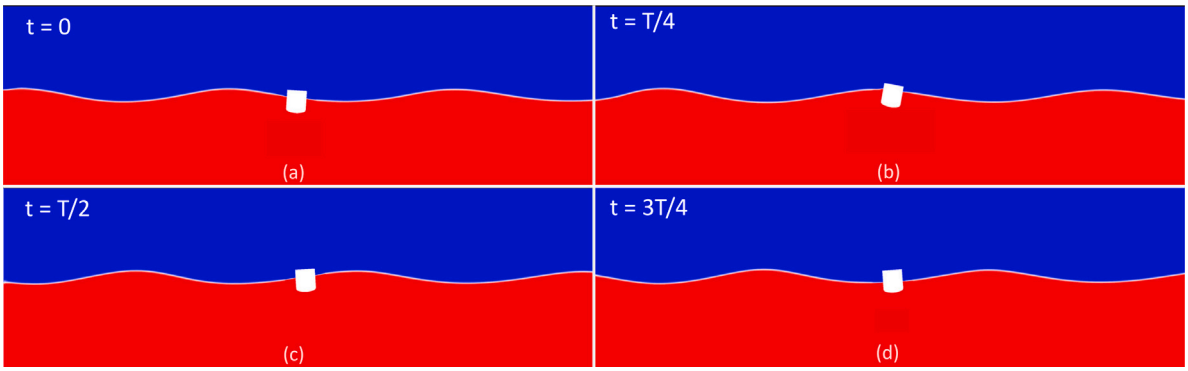

Fig. 16. WEC's response at four time instances during a wave cycle, when subjected to regular wave RW9 .

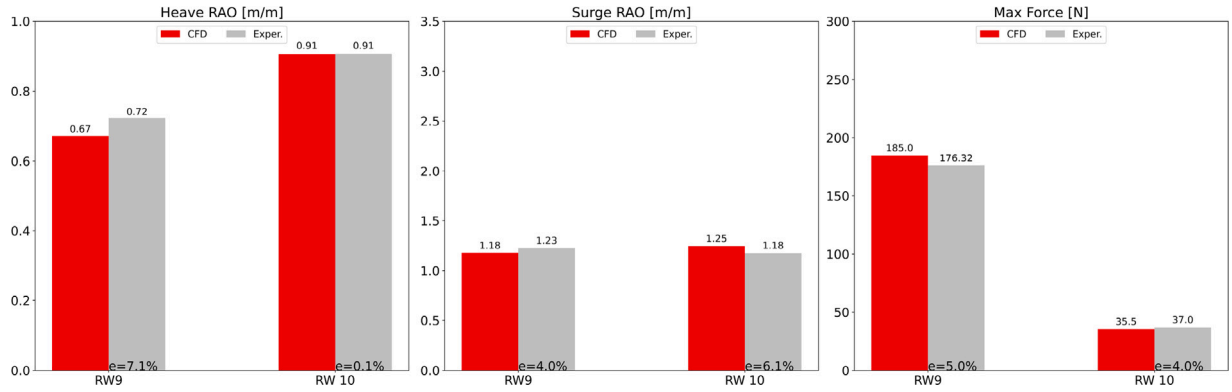

Fig. 17. Regular waves 9 and 10: The heave, surge RAOs and the max. mooring force, for the numerical simulations and experimental results.

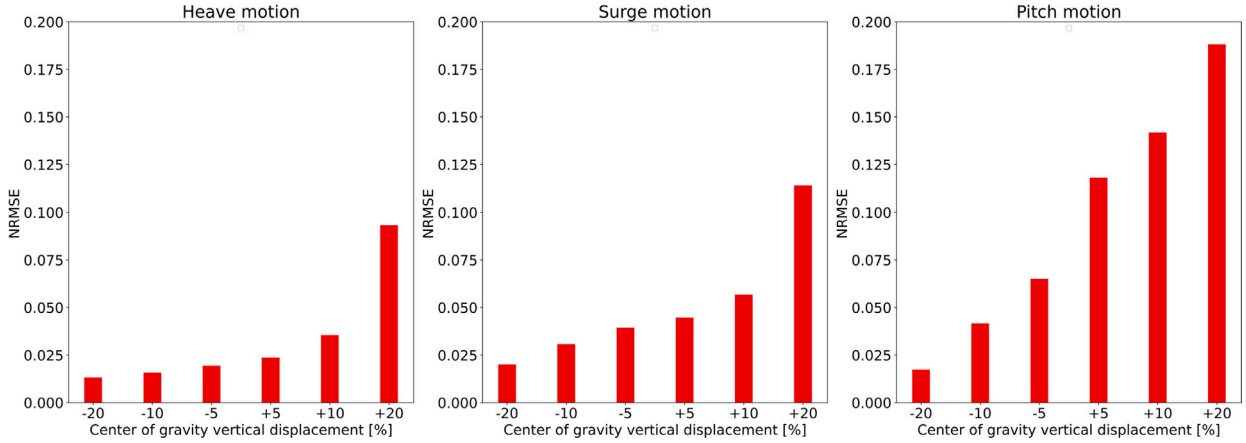

Fig. 18. Center of gravity (CoG) sensitivity study: The CoG is displaced by ± 5%, ± 10%, ± 20% from its initial position and the difference in the resulted motion response is expressed via the NRMSE metric.

steepness waves, while the deviation is kept below 10% in higher and steeper waves. The maximum mooring line force is estimated within an accuracy of 5% and 7% for smaller and higher steepness waves, respectively. However, the numerical model is not able to provide accurate solution for the pitch motion. This issue may rely on the uncertainty in the experimental characteristics, but as this study focuses on a point-absorber WEC, the contribution of the pitch motion is of secondary importance.

The developed high-fidelity CFD model of the point-absorber WEC subjected in 50-year return period waves is validated based on experimental campaign data. The model can be used for future assessment of the RAOs and the critical mooring loads under extreme wave conditions and supplement to a large extend the costly experimental campaigns.

CRediT authorship contribution statement

Eirini Katsidoniotaki: Conceptualization, Methodology, CFD simulations, Analysis of the results, Writing and Editing. **Zahra Shahroozi:** Experimental tests, Writing and Editing. **Claes Eskilsson:** Methodology, Analysis of the results and Editing. **Johannes Palm:** Methodology

and Writing. **Jens Engström:** Experimental tests and Editing. **Malin Göteman:** Conceptualization, Analysis of the results, Writing and Editing.

Declaration of competing interest

The authors declare that they have no known competing financial interests or personal relationships that could have appeared to influence the work reported in this paper.

Data availability

Data will be made available on request.

Acknowledgments

The research in this paper was supported by the Centre of Natural Hazards and Disaster Science, Sweden, the Swedish Research Council (VR, grant number 2015-04657), the Swedish Energy Authority (project number 47264-1). This scientific paper was also supported by the Onassis Foundation, scholarship ID: F ZP 021-1/2019-2020. The CFD simulations were performed on resources provided by the Swedish National Infrastructure for Computing (SNIC) at the HPC cluster: Tetralith at the National Supercomputer Centre, Linköping University. All authors have read and agreed to the published version of the manuscript.

References

Boström, C., 2011. Electrical Systems for Wave Energy Conversion (Ph.D. thesis). Acta Universitatis Upsaliensis.

Chen, W., Dolguntseva, I., Savin, A., Zhang, Y., Li, W., Svensson, O., Leijon, M., 2017. Numerical modelling of a point-absorbing wave energy converter in irregular and extreme waves. Appl. Ocean Res. 63, 90–105.

Chen, H., Qian, L., Ma, Z., Bai, W., Lin, Z., 2019. CCP-WSI blind test series 3: OpenFOAM simulation of focused wave interaction with a simplified wave energy converter. In: The 29th International Ocean and Polar Engineering Conference. OnePetro.

Choi, S.-H., Park, J.-O., Park, K.-S., 2017. Tension analysis of a 6-degree-of-freedom cable-driven parallel robot considering dynamic pulley bearing friction. Adv. Mech. Eng. 9 (8), 1687814017714981.

Clauss, G.F., Bergmann, J., 1986. Gaussian wave packets - a new approach to seakeeping tests of ocean structures. Appl. Ocean Res. 8 (4), 190–206.

Coe, R.G., Rosenberg, B.J., Quon, E.W., Chartrand, C.C., Yu, Y.-H., van Rij, J., Mundon, T.R., 2019. CFD design-load analysis of a two-body wave energy converter. J. Ocean Eng. Mar. Energy 5 (2), 99–117.

Domínguez, J.M., Crespo, A.J., Hall, M., Altomare, C., Wu, M., Stratigaki, V., Troch, P., Cappietti, L., Gómez-Gesteira, M., 2019. SPH simulation of floating structures with moorings. Coast. Eng. 153, 103560.

ESI, 2019. OpenFOAM v1906 release notes. [Online] https://www.openfoam.com/news/main-news/openfoam-v1906. (Accessed 07 February 2022).

Higuera, P., Lara, J.L., Losada, I.J., 2013. Realistic wave generation and active wave absorption for Navier–Stokes models: Application to OpenFOAM®. Coast. Eng. 71, 102–118.

Hinrichsen, P.F., 2014. Bifilar suspension measurement of boat inertia parameters. J. Sail. Technol. 3 (12), 1–37.

Hu, Z.Z., Greaves, D., Raby, A., 2016. Numerical wave tank study of extreme waves and wave-structure interaction using OpenFoam®. Ocean Eng. 126, 329–342.

Katsidoniatski, E., Yu, Y.-H., Goteman, M., 2021. Midfidelity Model Verification for a Point-Absorbing Wave Energy Converter with Linear Power Takeoff. Technical Report, National Renewable Energy Lab.(NREL), Golden, CO (United States).

Katsidoniotaki, E., Göteman, M., 2022. Numerical modeling of extreme wave interaction with point-absorber using OpenFOAM. Ocean Eng. 245, 110268.

Katsidoniotaki, E., Nilsson, E., Rutgersson, A., Engström, J., Göteman, M., 2021. Response of point-absorbing wave energy conversion system in 50-years return period extreme focused waves. J. Mar. Sci. Eng. 9 (3), 345.

Kramer, M.B., Andersen, J., Thomas, S., Bendixen, F.B., Bingham, H., Read, R., Holk, N., Ransley, E., Brown, S., Yu, Y.-H., et al., 2021. Highly accurate experimental heave decay tests with a floating sphere: A public benchmark dataset for model validation of fluid–structure interaction. Energies 14 (2), 269.

Madhi, F., Yeung, R.W., 2018. On survivability of asymmetric wave-energy converters in extreme waves. Renew. Energy 119, 891–909.

Neary, V.S., Lawson, M., Previsic, M., Copping, A., Hallett, K.C., Labonte, A., Rieks, J., Murray, D., 2014. Methodology for Design and Economic Analysis of Marine Energy Conversion (MEC) Technologies. Technical Report, Sandia National Lab. (SNL-NM), Albuquerque, NM (United States).

Palm, J., Eskilsson, C., 2021. Facilitating large-amplitude motions of wave energy converters in OpenFoam by a modified mesh morphing approach. In: 14th European Wave and Tidal Energy Conference 5-9th Sept 2021, Plymouth, UK. pp. 2107–1.

Palm, J., Eskilsson, C., Paredes, G.M., Bergdahl, L., 2016. Coupled mooring analysis for floating wave energy converters using CFD: Formulation and validation. Int. J. Mar. Energy 16, 83–99.

Ransley, E.J., Brown, S.A., Hann, M., Greaves, D.M., Windt, C., Ringwood, J., Davidson, J., Schmitt, P., Yan, S., Wang, J.X., et al., 2021. Focused wave interactions with floating structures: A blind comparative study. Proc. Inst. Civ. Eng. Eng. Comput. Mech. 174 (1), 46–61.

Ransley, E., Greaves, D., Raby, A., Simmonds, D., Jakobsen, M.M., Kramer, M., 2017. RANS-VOF modelling of the wavestar point absorber. Renew. Energy 109, 49–65.

Ransley, E., Yan, S., Brown, S., Hann, M., Graham, D., Windt, C., Schmitt, P., Davidson, J., Ringwood, J., Musiedlak, P.-H., et al., 2020. A blind comparative study of focused wave interactions with floating structures (CCP-WSI blind test series 3). Int. J. Offshore Polar Eng. 30 (01), 1–10.

Ransley, E., Yan, S., Brown, S.A., Mai, T., Graham, D., Ma, Q., Musiedlak, P.-H., Engsig-Karup, A.P., Eskilsson, C., Li, Q., et al., 2019. A blind comparative study of focused wave interactions with a fixed FPSO-like structure (CCP-WSI blind test series 1). Int. J. Offshore Polar Eng. 29 (02), 113–127.

Ropero-Giralda, P., Crespo, A.J., Tagliafierro, B., Altomare, C., Domínguez, J.M., Gómez-Gesteira, M., Viccione, G., 2020. Efficiency and survivability analysis of a point-absorber wave energy converter using DualSPHysics. Renew. Energy 162, 1763–1776.

Rusche, H., 2003. Computational Fluid Dynamics of Dispersed Two-Phase Flows at High Phase Fractions (Ph.D. thesis). Imperial College London (University of London).

Shahroozi, Z., Göteman, M., Engström, J., 2022. Experimental investigation of a point-absorber wave energy converter response in different wave-type representations of extreme sea states. Ocean Eng. 248, 110693.

Sjökvist, L., Wu, J., Ransley, E., Engström, J., Eriksson, M., Göteman, M., 2017. Numerical models for the motion and forces of point-absorbing wave energy converters in extreme waves. Ocean Eng. 145, 1–14.

Starling, M., 2009. Guidelines for Reliability, Maintainability and Survivability of Marine Energy Conversion Systems: Marine Renewable Energy Guides. European Marine Energy Centre.

van Rij, J., Yu, Y.-H., Guo, Y., Coe, R.G., 2019. A wave energy converter design load case study. J. Mar. Sci. Eng. 7 (8), 250.

van Rij, J., Yu, Y.-H., Tran, T.T., 2021. Validation of simulated wave energy converter responses to focused waves. Proc. Inst. Civ. Eng. Eng. Comput. Mech. 174 (1), 32–45.

Veritas, N., 2000. Environmental Conditions and Environmental Loads. Det Norske Veritas Oslo, Norway.

Weller, H., 2002. Derivation, Modelling and Solution of the Conditionally Averaged Two-Phase Flow Equations. Vol. 2. Nabla Ltd, No Technical Report TR/HGW, p. 9.

Weller, H.G., Tabor, G., Jasak, H., Fureby, C., 1998. A tensorial approach to computational continuum mechanics using object-oriented techniques. Comput. Phys. 12 (6), 620–631.

Windt, C., Davidson, J., Chandar, D.D., Faedo, N., Ringwood, J.V., 2020a. Evaluation of the overset grid method for control studies of wave energy converters in OpenFOAM numerical wave tanks. J. Ocean Eng. Mar. Energy 6 (1), 55–70.

Windt, C., Davidson, J., Ransley, E.J., Greaves, D., Jakobsen, M., Kramer, M., Ringwood, J.V., 2020b. Validation of a CFD-based numerical wave tank model for the power production assessment of the Wavestar ocean wave energy converter. Renew. Energy 146, 2499–2516.

Windt, C., Faedo, N., García-Violini, D., Peña-Sanchez, Y., Davidson, J., Ferri, F., Ringwood, J.V., 2020c. Validation of a CFD-based numerical wave tank model of the 1/20th scale Wavestar wave energy converter. Fluids 5 (3), 112.

Windt, C., Ringwood, J.V., Davidson, J., Schmitt, P., 2020d. CCP-WSI blind test series 3: CFD-based numerical wave tank experiments employing an impulse source wave maker. Int. J. Offshore Polar Eng. 30 (01), 28–35.

Yu, Y.-H., van Rij, J., Coe, R., Lawson, M., 2015. Preliminary wave energy converters extreme load analysis. In: International Conference on Offshore Mechanics and Arctic Engineering. Vol. 56574. American Society of Mechanical Engineers, V009T09A026.

Z. Shahroozi, J.E., 2021. Experimental results of force measurements from a scaled point absorbing wave energy converter subjected to extreme waves. In: Greaves, D. (Ed.), Proceedings of the Fourteenth European Wave and Tidal Energy Conference. EWTEC, University of Plymouth, UK, pp. 1881-1–1881-10. ISSN: 2309-1983.